Cancer Research

Image-Guided Breast Tumor Therapy Using a Small Interfering RNA Nanodrug

Mohanraja Kumar, Mehmet Yigit, Guangping Dai, Anna Moore, and Zdravka Medarova

Abstract

Iron oxide nanoparticles offer a feasible tool for combined imaging and delivery of small interfering RNA (siRNA) to tumors, stimulating active interest in exploring different imaging and delivery platforms suitable for detection by a variety of modalities. In this study, we describe the synthesis and testing of a tumor-targeted nanodrug (MN-EPPT-siBIRC5) that is designed to specifically shuttle siRNA to human breast tumors. The nanodrug binds the tumor-specific antigen uMUC-1, which is found in >90% of human breast adenocarcinomas. MN-EPPT-siBIRC5 consists of superparamagnetic iron oxide nanoparticles [for magnetic resonance imaging (MRI)], the dye Cy5.5 (for near-IR optical imaging), peptides (EPPT) that specifically target uMUC-1, and a synthetic siRNA that targets the tumor-specific antiapoptotic gene *BIRC5*. Nanodrug uptake by human breast adenocarcinoma cells resulted in a significant downregulation of *BIRC5*. Following i.v. delivery into subcutaneous mouse models of breast cancer, the nanodrug showed a preferential tumor uptake, which could be visualized by MRI and near-IR optical imaging. Furthermore, MRI could be used to quantitatively monitor nanodrug bioavailability in the tumor tissue throughout the course of treatment. Intravenous injection of the agent once a week over 2 weeks resulted in the induction of considerable levels of necrosis and apoptosis in the tumors, translating into a significant decrease in tumor growth rate. Our strategy permits the simultaneous tumor-specific delivery of siRNA to tumors and the imaging of the delivery process. More generally, it illustrates the potential to apply this approach to many human cancer studies, including for basic tumor biology and therapy. *Cancer Res; 70(19); 7553–61. ©2010 AACR.*

Introduction

RNA interference (RNAi) holds considerable potential as a molecular therapeutic tool due to its broad applicability and exquisite specificity (1–3). The main hurdle to the application of RNAi *in vivo* is the difficulty in achieving efficient delivery of the small interfering RNA (siRNA) to the target tissue due to phenomena such as RNase degradation, interaction with blood components, and inefficient translocation across the cell membrane. To address these obstacles, many approaches have been proposed for *in vivo* siRNA delivery. They include liposome-mediated delivery of siRNA in stable nucleic acid–lipid particles (4), polymer-based delivery using atelocollagen and chitosan (5, 6), conjugation to cholesterol (7, 8), and complexing with positively charged peptides or proteins (9–11), to name a few. Various nanoparticle carriers have been proposed for siRNA delivery *in vitro* (12–14) and *in vivo* (refs. 15, 16; also reviewed in ref. 17).

To evaluate the success of siRNA-mediated therapy, it is also very important to monitor its bioavailability following *in vivo* administration as well as the associated therapeutic effect because this will help to develop more successful delivery strategies. In this regard, noninvasive imaging plays an important role as a technology that permits the *in vivo* monitoring of siRNA delivery.

Magnetic resonance imaging (MRI) represents a suitable modality for this purpose because it is characterized by a high spatial resolution, tomographic capability, and the potential to provide quantitative information about contrast agent abundance in tissue (18). At present, few reports have described the application of MRI for image-guided siRNA delivery *in vitro* (19) and *in vivo* (20–22).

Previously, we have shown the feasibility of MRI-guided siRNA delivery to tumors using myristoylated polyarginine-conjugated magnetic nanoparticles (MN) that accumulate in tumor tissue through enhanced permeability and retention effect (20). Despite their capability to mediate very efficient silencing *in vivo*, these nanoparticles exhibited a high degree of nonspecific uptake, especially by the liver, leading to a more rapid degradation and a reduced effective dose of the agent at the tumor site. A more biologically relevant approach toward improving the bioavailability of the siRNA complex would involve the implementation of a tumor-targeted

Authors' Affiliation: Molecular Imaging Laboratory, MGH/HST Athinoula A. Martinos Center for Biomedical Imaging, Department of Radiology, Massachusetts General Hospital/Harvard Medical School, Boston, Massachusetts

Note: Supplementary data for this article are available at Cancer Research Online (http://cancerres.aacrjournals.org/).

Corresponding Author: Zdravka Medarova, Molecular Imaging Laboratory, MGH/MIT/HMS Athinoula A. Martinos Center for Biomedical Imaging, Department of Radiology, Massachusetts General Hospital/Harvard Medical School, Building 75, 13th Street, Charlestown, MA 02129. Phone: 617-643-4889; Fax: 617-643-4865; E-mail: zmedarova@partners.org.

doi: 10.1158/0008-5472.CAN-10-2070

design. This is a necessary step to transform our original delivery agent into an effective, clinically relevant nanodrug.

In the present study, we address this issue by constructing a tumor-selective probe (MN-EPPT-siBIRC5), which consists of MN (for MRI), labeled with near-IR dye Cy5.5 (for optical imaging) and conjugated to a peptide (EPPT), which targets the tumor-specific antigen uMUC-1, as well as to siRNA against the antiapoptotic gene *birc5*, which encodes survivin. We have previously established the *in vivo* tumor-targeting properties of the MN-EPPT platform in a variety of adenocarcinoma models, including breast cancer (23–25). Our present results show the application of this platform for the efficient image-guided delivery of siRNA to breast tumors and the mediation of a robust therapeutic effect, illustrating the potential of this agent as a novel cancer nanodrug.

Materials and Methods

Nanodrug synthesis

The EPPT peptide was synthesized by general Fmoc chemistry using 2-6*H*-benzotriazole-1-yl-9,1,3,3-tetramethylammonium hexafluorophosphate and 1-hydroxybenzotriazole activating agents. Amino acids and resin were purchased from EMD Chemicals. All other reagents were purchased from Advanced Chemtech, Sigma-Aldrich, GE Life Sciences, and Fisher Scientific and used without further purifications. The sequence Cys-$(PEG)_2$-Tyr-Cys(Acm)-Ala-Arg-Glu-Pro-Pro-Thr-Arg-Thr-Phe-Ala-Tyr-Trp-Gly-Lys(FITC)-$CONH_2$ (EPPT) was synthesized in a 0.1 mmol scale of rink amide methylbenzyl hydroamine resin. The Lys (Dde) side chain on the resin was selectively cleaved using 2% hydrazine in dimethylformamide and coupled with FITC. Finally, the resin was cleaved by 5 mL of cocktail mixture [81.5% trifluoroacetic acid (TFA), 5% thioanisole, 5% phenol, 5% water, 2.5% ethanedithiol, and 1% triisopropylsilane], precipitated in cold ether, purified by high-performance liquid chromatography using eluting solvents A and B (A = 0.1% TFA in 95% water + 5% acetonitrile and B = 0.1% TFA in 90% acetonitrile + 10% water), and characterized by matrix-assisted laser desorption/ionization mass spectrometry (2,827.17 calculated and 2,828.60 found).

The parental MNs (cross-linked dextran-coated superparamagnetic iron oxide nanoparticles) were synthesized as described (26).

The subsequent steps are outlined in Fig. 1A. The MN-Cy5.5 precursor was synthesized as described (23, 25). The targeting EPPT peptide was coupled to MN-Cy5.5 for the resultant MN-EPPT precursor probe using a protocol modified from previous reports (23, 25). Briefly, the nanoparticles were

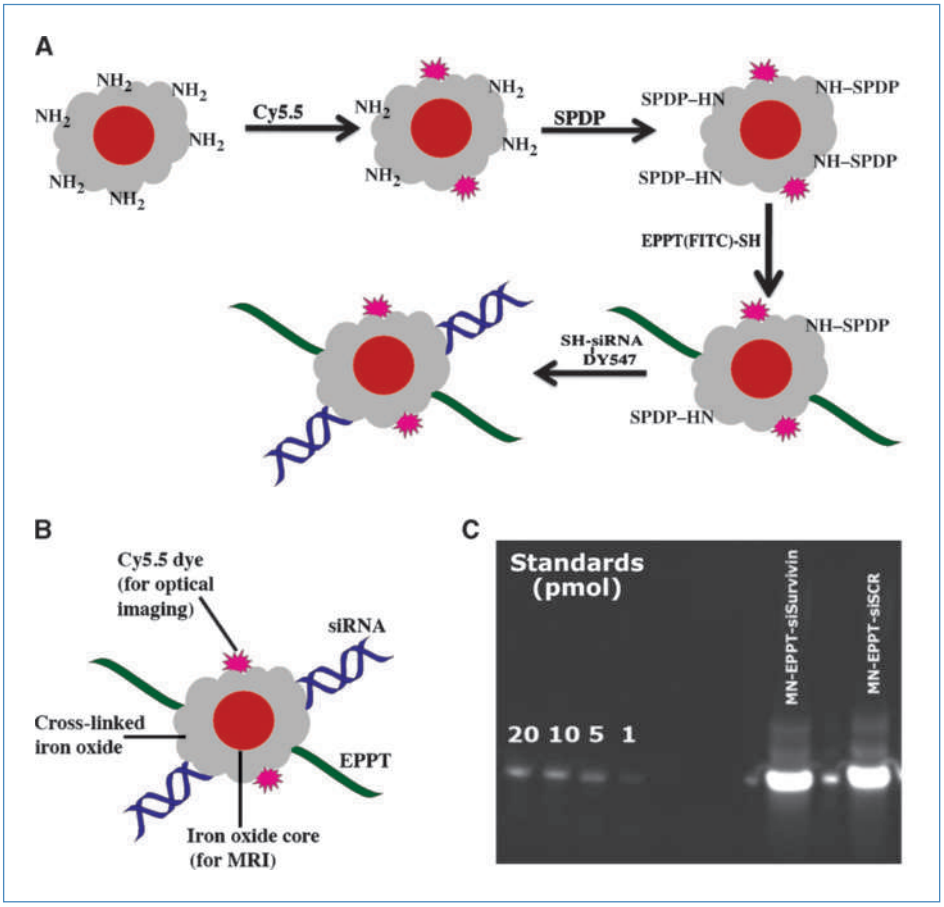

Figure 1. Synthesis and characterization of MN-EPPT-siRNA. A, flowchart of the synthesis. B, nanodrug characterization. The nanodrug consisted of dextran-coated MNs triple labeled with Cy5.5 dye, EPPT peptides, and synthetic siRNA duplexes. C, gel electrophoresis showing dissociation of siRNAs from the nanoparticles under reducing conditions.

conjugated to the heterobifunctional cross-linker *N*-succinimidyl 3-(2-pyridyldithio) propionate (Pierce Biotechnology), and the product was purified using a Sephadex PD-10 column (GE Life Sciences) against a 100 mmol/L sodium phosphate solution (pH 8.1). The peptide EPPT was attached to this linker via the sulfhydryl reactive pyridyl disulfide residue in a 100 mmol/L sodium phosphate solution (pH 8.1).

The siRNA oligos were then conjugated to MN-EPPT using a protocol modified from previous reports (20, 27). 5′-Sense thiol-modified *birc5*-targeting and scrambled siRNA duplexes were designed and synthesized by Dharmacon. For conjugation, the siRNA was deprotected before coincubation with the MNs, as recommended by the supplier (Dharmacon). Briefly, the duplex was deprotected with a solution of 3% Tris (2-carboxy-ethyl)-phosphin-HCl followed by a 9.5 mol/L ammonium acetate/ethyl alcohol precipitation. Following deprotection and precipitation, the siRNA was dissolved in 50 mmol/L NaCl and 10 mmol/L EDTA (pH 8) and incubated with the MNs overnight at 4°C. The final nanodrug was purified using a G-50 Sephadex Quick Spin column (Roche Applied Science).

Nanodrug characterization

The nanoparticle concentration was determined based on iron concentration and measured spectrophotometrically, as described (28). The conjugation ratio of Cy5.5 and EPPT-FITC to MN was quantified spectrophotometrically, as described (16). The number of EPPT-FITC peptides and Cy5.5 molecules per nanoparticle was obtained from absorbance at 494 nm [extinction coefficient, 68,000 $(mol/L)^{-1}$ cm^{-1}] and 678 nm [extinction coefficient, 250,000 $(mol/L)^{-1}$ cm^{-1}], respectively. To characterize the conjugation efficiency and dissociation stoichiometry of siRNA from MN, we performed gel electrophoresis of MN-EPPT-siRNA, following incubation in the reducing buffer DTT (100 mmol/L DTT for 1 hour at 37°C). The siRNA standard and the nanodrug treated with the reducing agent were electrophoresed on a 15% Tris-borate EDTA gel (Invitrogen) at 200 V for 45 minutes. After electrophoresis, the gel was stained with 0.5 μg/mL ethidium bromide for 30 minutes and visualized using a Molecular Imager FX scanner (Bio-Rad). The images were analyzed using the software Quantity One, version 4.4.0 (Bio-Rad).

Cell line

All of the studies were performed using the BT-20 and/or CAPAN-2 and LS-174T cell lines [human breast, pancreatic, and colorectal adenocarcinoma; American Type Culture Collection (ATCC) HTB-19, HTB-80, and CL-188, respectively]. The cell lines were authenticated based on viability, recovery, growth, morphology, and isoenzymology by the supplier (ATCC).

Flow cytometry

Nanodrug uptake by BT-20, CAPAN-2, and LS-174T cells was analyzed using flow cytometry. Cells were incubated with MN-EPPT-siBIRC5 for 48 hours at 37°C, washed, and analyzed in the FL4 channel (Cy5.5, MN) and the FL2 channel (Dy547, siRNA). To correlate nanodrug uptake to uMUC-1 expression, after incubation with the nanodrug, the cells were fixed in 2% paraformaldehyde, incubated for 1 hour at 4°C with a uMUC-1–specific monoclonal antibody (FITC-labeled mouse anti-human CD227; BD Biosciences), and analyzed in the FL4 channel (Cy5.5, MN) and the FL1 channel (FITC, uMUC-1–specific antibody). Flow cytometry was performed using a FACSCalibur (Becton Dickinson) equipped with the CellQuest software package (Becton Dickinson).

MRI of cell phantoms

BT-20 cells were treated as described for flow cytometry. The cells were then pelleted in 0.2 mL PCR tubes and imaged. Imaging was performed using a 9.4-T Bruker horizontal bore scanner equipped with ParaVision 3.0 software. The imaging protocol consisted of coronal T2-weighted spin echo (SE) pulse sequences with the following parameters: SE repetition time/echo time (TE) = 3,000/[8, 16, 24, 32, 40, 48, 56, 64]; field of view = 32 × 32 mm; matrix size = 128 × 128 pixels; slice thickness = 0.5 mm; in-plane resolution = 250 × 250 μm^2. Image reconstruction and analysis were performed using the Marevisi 3.5 software (Institute for Biodiagnostics, National Research Council, Canada). T2 maps were constructed according to established protocol by fitting the T2 values for each of the eight TEs to a standard exponential decay curve.

T2 relaxation times were calculated by manually segmenting out the cell pellet on MR images.

Real-time quantitative reverse transcription-PCR

To assess *birc5* knockdown by the nanodrug, BT-20, CAPAN-2, and LS-174T cells were incubated with MN-EPPT-siBIRC5 or the control MN-EPPT-siSCR (100 μg/mL iron) for 48 hours at 37°C. Total RNA was extracted using the RNeasy Mini kit, according to the manufacturer's protocol (Qiagen, Inc.). Relative levels of uMUC-1 mRNA were determined by real-time quantitative reverse transcription-PCR (qRT-PCR; Taqman protocol). Taqman analysis was performed using an ABI Prism 7700 sequence detection system (PE Applied Biosystems). The PCR primers and Taqman probe specific for MUC-1 mRNA were designed using Primer Express software 1.5. Primer and probe sequences were as follows:

forward primer, 5′-ACAGGTTCTGGTCATGCAAGC-3′ (nucleotides 64–84 in the 5′ nonrepetitive region);
reverse primer, 5′-CTCACAGCATTCTTCTCAGTAGAGCT-3′ (nucleotides 139–164 in the 5′ nonrepetitive region); and
Taqman probe, 5′-FAM-TGGAGAAAAGGAGACTTCGGC-TACCCAGA-TAMRA-3′ (nucleotides 96–124 in the 5′ nonrepetitive region).

Eukaryotic 18S rRNA Taqman PDAR Endogenous Control reagent mix (PE Applied Biosystems) was used to amplify 18S rRNA as an internal control, according to the manufacturer's protocol.

Tumor model

Five- to-6-week-old female *nu/nu* mice ($n = 8$; Massachusetts General Hospital Radiation Oncology breeding facilities) were injected s.c. with 3×10^6 BT-20 tumor cells (ATCC). Animals were used in experiments on days 10 to 14 after the inoculation, when tumors were ~0.5 cm in diameter.

All animal experiments were performed in compliance with institutional guidelines and according to the animal protocol approved by the Subcommittee on Research Animal Care at Massachusetts General Hospital.

Animal treatment

Treatment with MN-EPPT-siBIRC5 or the control MN-EPPT-siSCR probe involved systemic administration through the tail vein at a dose of 10 mg/kg Fe and 400 nmol/kg siRNA once a week over the course of 2 weeks. Based on our previous biodistribution data (23), the amount of probe/siRNA delivered to the tumor with each injection is ~2 mg/kg Fe, which is equivalent to ~ 8 nmol/kg siRNA.

In vivo MRI

MRI was performed before and 24 hours after each nanodrug injection using a 9.4-T Bruker horizontal bore scanner equipped with ParaVision 3.0 software. The imaging sequences were the same as for *in vitro* MRI. Image reconstruction and analysis were performed as described for *in vitro* MRI.

Tumor volumes and T2 relaxation times were calculated by manually segmenting out the tumor on MR images. Quantitative evaluation of differential tumor growth by MRI was based on multislice T2-weighted images. The volume was estimated by adding up the number of voxels occupied by tumor and multiplying by voxel volume. For T2 map analysis of relaxation times, the terminal slices were not included to avoid interference from partial volume effects.

In vivo and *ex vivo* optical imaging

In vivo optical imaging was performed immediately after each MRI session.

Animals were placed prone into a whole-body animal imaging system (IVIS Spectrum, Caliper Life Sciences), equipped with 10 narrow band excitation filters (30-nm bandwidth) and 18 narrow band emission filters (20-nm bandwidth) that assist in significantly reducing autofluorescence by the spectral scanning of filters and the use of spectral unmixing algorithms (Caliper Life Sciences). Imaging was performed using a 675-nm excitation and a 720-nm emission filter. The fluorescence imaging settings (exposure time, 0.5 seconds; F-stop, 2; binning, medium) were kept constant for comparative analysis. Grayscale white-light photographs and epifluorescent images were acquired and superimposed. For *ex vivo* imaging, excised tumors and adjacent muscle tissue were placed in the optical imaging system and imaged as above. The images were reconstructed using the Living Image software version 3.1 (Caliper Life Sciences).

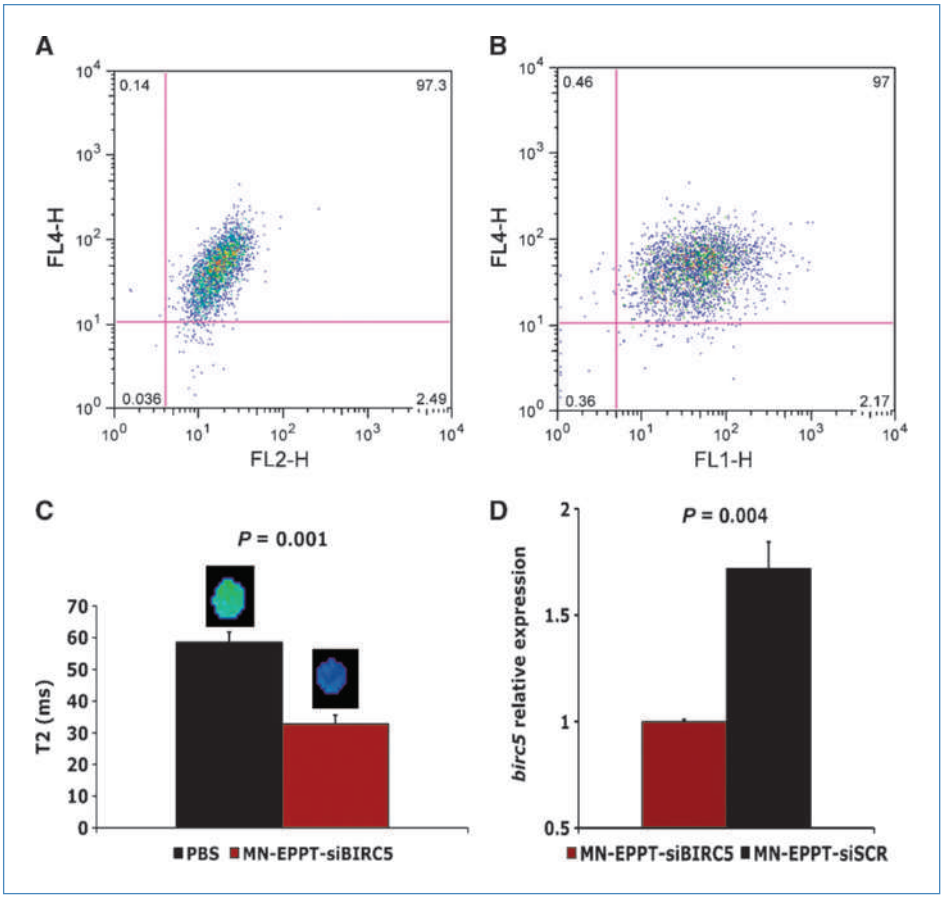

Figure 2. *In vitro* testing of MN-EPPT-siRNA uptake and silencing efficacy in BT-20 human breast adenocarcinoma cells. A, flow cytometry to assess nanodrug uptake. Representative FL2 (Dy547, siRNA) versus FL4 (Cy5.5, MN) dot plots showing that 97.9 ± 0.8% of the cells were labeled with the nanodrug. The good cellular colocalization between fluorescence in the two channels indicated stability of the nanodrug. B, flow cytometry to assess nanodrug uptake as a function of uMUC-1 positivity. The cellular colocalization between fluorescence in the FL4 (Cy5.5, MN) and FL1 (FITC, uMUC-1–specific antibody) channels suggested that the nanodrug uptake by the cells is representative of uMUC-1 abundance. C, *in vitro* T2-weighted MRI. There was a significant shortening of the T2 relaxation times of the cells incubated with MN-EPPT-siBIRC5 relative to PBS-incubated controls, suggesting that the cellular uptake of the nanodrug could be detected by MRI. D, qRT-PCR of human breast adenocarcinoma cells incubated with MN-EPPT-siBIRC5 or control probes. There was a significant knockdown of *birc5* mediated by MN-EPPT-siBIRC5 relative to the MN-EPPT-siSCR control ($P = 0.004$; $n = 4$).

Immunohistochemistry and *in situ* apoptosis detection

To detect the nanodrug in tumor tissues, tumors were embedded in Tissue-Tek OCT compound (Sakura Finetek) and snap frozen in liquid nitrogen. Tumors were then cut into 7-μm frozen sections, fixed in 2% paraformaldehyde, washed, counterstained with Vectashield mounting medium with 4′,6-diamidino-2-phenylindole (DAPI; Vector Laboratories), and analyzed by fluorescence microscopy. Microscopy was performed using a Nikon Eclipse 50i fluorescence microscope equipped with an appropriate filter set (Chroma Technology Corp.). Images were acquired using a charge-coupled device camera with near-IR sensitivity (SPOT 7.4 Slider RTKE; Diagnostic Instruments) and analyzed using SPOT 4.0 advanced version software (Diagnostic Instruments). Fluorescence was collected in the green channel for detection of the FITC label on EPPT peptides, the blue channel for DAPI, and the NIR channel for detection of the Cy5.5 label on MN nanoparticles.

To evaluate levels of apoptosis in tumor cells, we performed a terminal deoxynucleotidyl transferase–mediated dUTP nick end labeling (TUNEL) assay (ApopTag Fluorescein *In situ* Apoptosis Detection kit, Chemicon International) according to the manufacturer's protocol. The nuclei were counterstained with DAPI and examined in the DAPI (nuclei) and FITC (apoptotic nuclei) channels. For quantitative analysis of apoptotic levels, a total of 100 nuclei over two separate slides were taken into account. To evaluate levels of necrosis, we stained sections with H&E and analyzed them by light microscopy.

Statistical analysis

All data were represented as means ± SD. Statistical analysis was performed using two-tailed Student's t test and linear regression where indicated. A P value of ≤0.05 was considered statistically significant.

Results

MN-EPPT-siRNA synthesis

The MN-EPPT-siRNA (BIRC5/SCR) probes consisted of dextran-coated MNs, triple conjugated to Cy5.5, EPPT, and siRNA (Fig. 1B). A ratio of four Cy5.5 molecules and eight EPPT peptides per nanoparticle was obtained. To characterize the conjugation efficiency and dissociation stoichiometry of siRNA from MN, we performed gel electrophoresis of MN-EPPT-siRNA, following incubation in the reducing buffer DTT. The resultant siRNA/MN molar ratios reached 7 for MN-EPPT-siBIRC5 and 7.15 for MN-EPPT-siSCR (Fig. 1C).

In vitro uptake and silencing efficacy of MN-EPPT-siBIRC5

To assess the cellular uptake of MN-EPPT-siBIRC5 by human BT-20 breast adenocarcinoma cells, we performed flow cytometry following incubation with the nanodrug. A representative dot plot is shown in Fig. 2A. A considerable 97.9 ± 0.8% of the cells were labeled with MN-EPPT-siBIRC5. The good cellular colocalization between fluorescence in the FL2 channel (Dy547, siRNA) and the FL4 channel (Cy5.5, MN) indicated stability of the nanodrug on cellular uptake. In addition, to show that the uptake is governed by the expression of MUC-1, we costained the cells with a MUC-1–specific monoclonal antibody. The cellular colocalization between fluorescence in the FL1 channel (MUC-1, FITC) and the FL4 channel (Cy5.5, MN) suggested MUC-1–specific uptake (Fig. 2B). Similar results were obtained with human pancreatic and colorectal adenocarcinoma cell lines (Supplementary Fig. S1A and B), illustrating the broad applicability of our approach.

Because one of our primary goals is to detect nanodrug bioavailability by MRI, we performed *in vitro* T2-weighted MRI on breast cancer cells, following incubation with MN-EPPT-siBIRC5. Quantitative analysis revealed a significant (P = 0.001, n = 4) shortening of the T2 relaxation times of the cells following incubation with the nanodrug, indicating that the uptake can be visualized and quantified by MRI

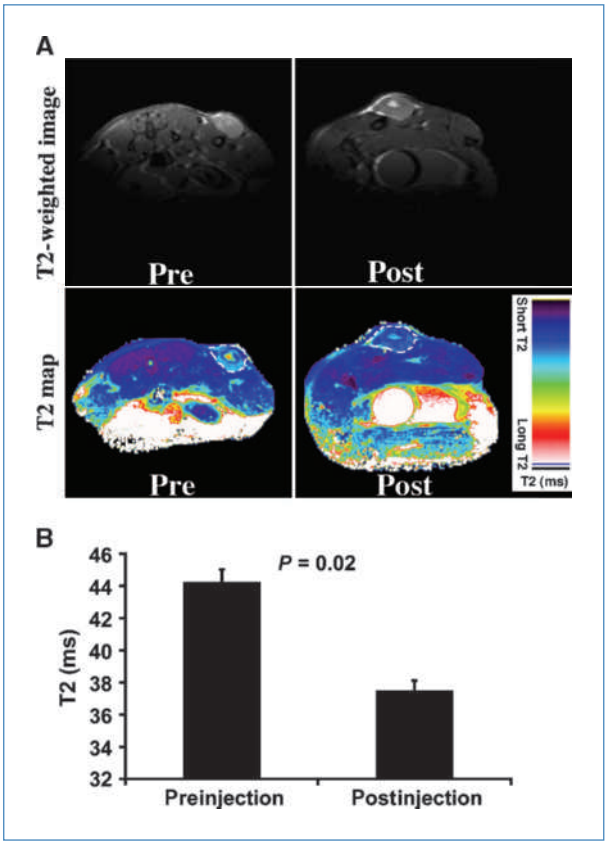

Figure 3. *In vivo* MRI in a subcutaneous breast tumor model. A, representative precontrast and postcontrast T2-weighted images (top) and color-coded T2 maps (bottom) of tumor-bearing mice injected i.v. with MN-EPPT-siBIRC5 (10 mg/kg iron). The tumors (outlined) were characteristically bright (T2 long) before contrast. At 24 h after injection, there was a loss of signal intensity (T2 shortening) associated with the tumors, indicative of nanodrug accumulation. B, quantitative analysis of tumor T2 relaxation times. T2 map analysis revealed a marked shortening of tumor T2 relaxation times 24 h after nanodrug injection, indicating accumulation of MN-EPPT-siBIRC5.

(Fig. 2C). Finally, to see if MN-EPPT-siBIRC5 can mediate effective silencing of the target gene, we isolated total RNA from the breast adenocarcinoma cell lines 48 hours after incubation with the nanodrug and performed quantitative gene expression analysis (qRT-PCR). As seen in Fig. 2D, treatment with MN-EPPT-siBIRC5 led to a significantly lower expression of *birc5* (survivin) relative to the siRNA scrambled, MN-siSCR, probe ($P = 0.004$, $n = 4$). Analogous levels of silencing were also seen in human pancreatic and colorectal adenocarcinoma cells (Supplementary Fig. S1C). These findings imply that the MUC-1 tumor antigen–targeted approach to siRNA delivery mediates a robust gene silencing effect.

In vivo imaging of MN-EPPT-siBIRC5 delivery to tumors

To monitor the delivery of the nanodrug to tumors, we performed *in vivo* MRI of mice, implanted s.c. with human breast adenocarcinoma tumors. Superparamagnetic iron oxide nanoparticles are characterized by their strong T2 magnetic susceptibility effects. Their presence in tissue is reflected by marked shortening of T2 relaxation times, resulting in a loss of signal (darkening) on MR images. In this experiment, tumors appeared characteristically bright on precontrast T2 images. Following injection of the nanodrug, there was a notable decrease in T2 relaxation time (signal) associated with the tumors (Fig. 3A), as a result of MN-EPPT-siBIRC5 accumulation. We also monitored tumor T2 relaxation times as a quantitative measure of nanodrug abundance in tumor tissue during the entire course of therapy. Treatment with the nanodrug involved weekly i.v. injections over the course of 2 weeks. Imaging was performed before and after each injection for a total of four data points. As shown in Fig. 3B, injection of the nanodrug resulted in a significant decrease of tumor T2 relaxation times ($P = 0.02$, $n = 4$). Furthermore, after injection, tumor T2 relaxation times remained significantly lower than the preinjection values at all time points (preinjection, 44.2 ± 0.8; postinjection range, 37.5 ± 0.6 to 28.1 ± 4.2; $P < 0.02$; $n = 4$), indicating that the selected treatment time course ensured persistence of the nanodrug in tumor tissue throughout the experiment.

Independent macroscopic confirmation of nanodrug delivery to the tumors was obtained by near-IR optical imaging of the same animals immediately after each MRI session. The Cy5.5 near-IR dye attached to MN allowed for the generation of near infrared fluorescence signal sufficient to detect the tumor-selective delivery of the nanodrug to the tumors (Fig. 4A). These findings were further corroborated by *ex vivo* imaging of excised tumors. The strong fluorescence associated with the tumors, but not with adjacent muscle tissue, indicated preferential accumulation of the nanodrug in the tumors (Fig. 4B).

The tumoral uptake observed by MRI and optical imaging was characteristic of both MN-EPPT-siBIRC5 and MN-EPPT-siSCR, as expected, based on the fact that both are targeted to uMUC-1 through the EPPT peptide (Supplementary Fig. S2). Quantitative MRI T2 map analysis revealed that there were no significant differences between the tumor T2 relaxation times of animals injected with MN-EPPT-siBIRC5 or MN-EPPT-siSCR at any treatment time point ($P > 0.05$; $n = 4$). This indicated that any phenotypic effects associated with MN-EPPT-siBIRC5 administration are a function of siRNA activity and are not influenced by a potential differential probe bioavailability.

Finally, to analyze the uptake of the nanodrug by tumor cells following *in vivo* delivery, we performed fluorescence microscopy of frozen tumor sections. The good colocalization between signal originating from the Cy5.5 label on MN and the FITC label on the EPPT peptide indicated that the nanodrug remained intact after persistence in the circulation (Fig. 4C). Taken together, these findings attested to the favorable

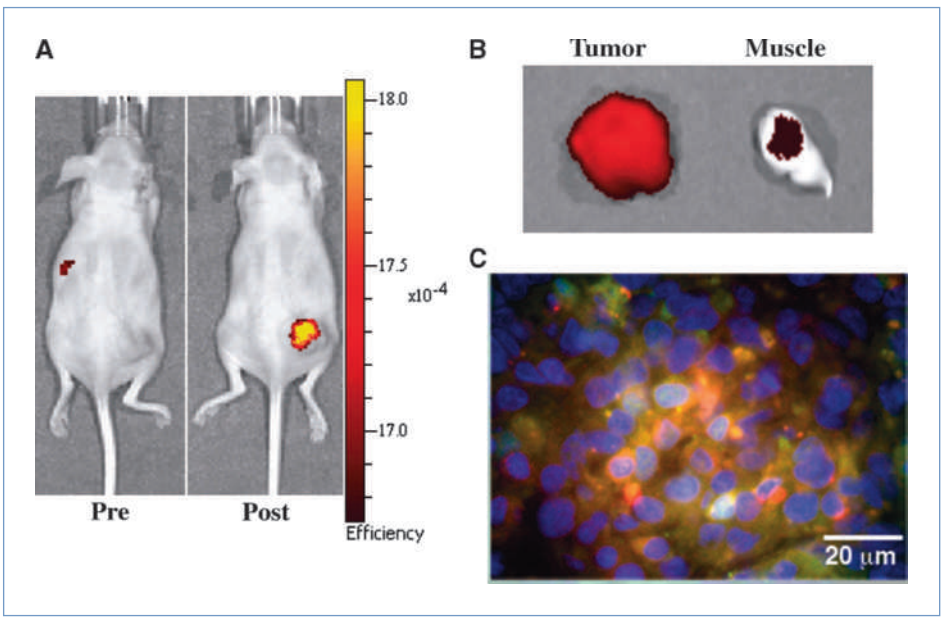

Figure 4. Optical imaging in a subcutaneous breast tumor model. A, *in vivo* imaging. The bright near-IR signal, associated with the tumors compared with surrounding tissue, reflected tumor-selective delivery of MN-EPPT-siBIRC5. B, *ex vivo* imaging. There was a bright near-IR fluorescence associated with the tumors. By contrast, the fluorescence of adjacent muscle tissue was at background levels. C, fluorescence microscopy. The colocalization between fluorescence in the green (FITC, EPPT) and near-IR (red, Cy5.5, MN) channels reflected the integrity of the nanodrug after persistence in the circulation. The tissues were counterstained with DAPI (nuclei, blue).

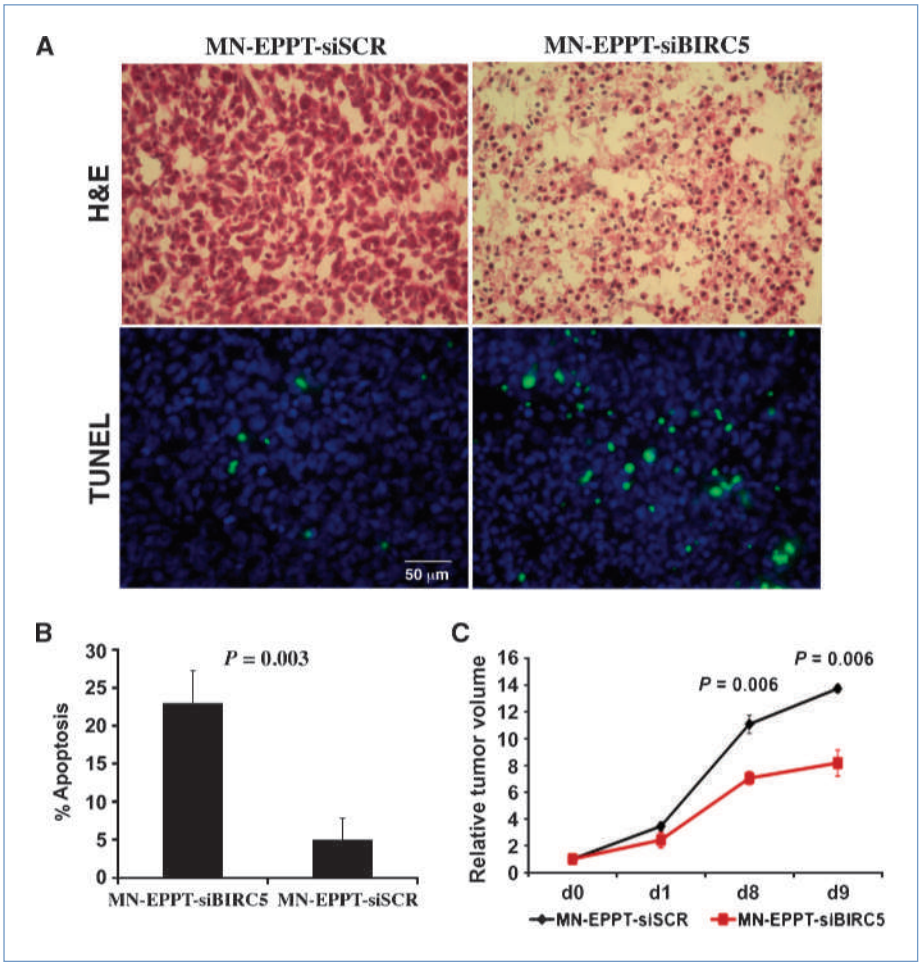

Figure 5. MN-EPPT-siBIRC5 therapeutic effects. A, H&E (top) and TUNEL (bottom) staining of tumor tissue from mice treated with MN-EPPT-siBIRC5 or MN-EPPT-siSCR. In the H&E sections, there were extensive eosinophilic areas in the experimental but not control tumors, suggesting the induction of necrosis by the siBIRC5-bearing nanodrug. There was a visible increase in the fraction of apoptotic (green) nuclei in the TUNEL-stained tissues from experimental mice relative to controls, indicating the induction of apoptosis. The tissues were counterstained with DAPI (nuclei, blue). B, quantitative analysis of the TUNEL experiments. There was a 5-fold induction of apoptosis in the tumor tissues of experimental animals relative to controls ($P = 0.003$). C, relative tumor volume measurements of MN-EPPT-siBIRC5– and MN-EPPT-siSCR–injected animals over the course of treatment. There was a significant decrease in tumor growth rate in the experimental animals relative to controls, apparent by 8 d after the beginning of treatment ($P < 0.01$; $n = 4$).

bioavailability of MUC-1–targeted MN-siRNAs delivered as part of the MN complex. They showed that the MN-EPPT-siRNA nanodrug successfully targeted tumors and that this process could be detected by *in vivo* MRI and optical imaging.

Therapeutic effects of MN-EPPT-siBIRC5 delivery to tumors

Because *birc5* encodes the antiapoptotic survivin proto-oncogene, silencing of *birc5* can mediate a therapeutic effect by inducing necrotic/apoptotic tumor cell death. We tested the therapeutic potential of MN-EPPT-siBIRC5 by H&E staining (necrosis) and TUNEL assay (apoptosis) of tumor sections derived from breast tumor–bearing animals treated with the nanodrug. We observed the induction of considerable levels of both necrosis (Fig. 5A) and apoptosis (Fig. 5A and B). There was a 5-fold increase in the fraction of apoptotic nuclei in experimental tumors versus controls injected with MN-EPPT-siSCR ($P = 0.003$; Fig. 5B). This translated into a ~2-fold decrease in tumor growth rate (Fig. 5C). Because there were no differences in the uptake of MN-EPPT-siBIRC5 and MN-EPPT-siSCR (Supplementary Fig. S2), we concluded that the therapeutic effect observed here was due to siBIRC5 action. These data indicated that the siRNA oligo remained functional *in vivo* as part of the MN-EPPT-siRNA complex, and illustrated the potential of this technology for tumor therapy.

Discussion

The discovery of the RNAi mechanism of posttranscriptional gene regulation (29) and its relevance to mammalian gene silencing (30) opened up a new possibility for intervention against disease. Therapeutic strategies that rely on RNAi are unique because they would involve the modular design of RNA duplexes capable of mediating powerful phenotypic reprogramming over a broad range of disease applications and with specificity sufficient to correct single-nucleotide mutations. The interest in developing RNAi into a therapeutic modality has engendered a variety of ideas and approaches that have as their final goal the transformation of the siRNA duplex into a molecular drug. Several of these approaches are undergoing clinical trials (31).

Our review of the literature, however, reveals the apparent lack of clinically relevant image-guided strategies for siRNA-based therapy. Although versatile, most nanoparticle delivery systems do not possess imaging capability. We feel that the "image-guided" property is important because imaging could

provide key information about the persistence of the agent in the circulation, its relative accumulation in the target tissue, and the associated phenotypic or therapeutic effect.

Here, we illustrate the potential of this approach by designing a tumor-targeted, imaging-capable nanodrug and applying it for MRI-guided breast tumor treatment in a murine xenograft model of the disease. MRI serves the dual purpose of reporting on the relative accumulation of the nanodrug in tumor tissue, as a guide to selecting an optimal treatment time course, and quantifying the change in tumor volume over the course of treatment, as an indicator of therapeutic response.

In addition to being detectable by MRI, our nanodrug is tumor targeted. Tumor targeting is deemed necessary to achieve optimized tumoral bioavailability and a minimized nonspecific uptake by vital organs. The tumor selectivity of our nanodrug derives from the tumor-associated uMUC-1 antigen, which is underglycosylated and overexpressed in >90% of breast cancers and in >50% of all cancers in humans (32), attesting to the broad applicability of this delivery strategy.

As a therapeutic moiety, we have used siRNA to the human *BIRC5* gene. *BIRC5* encodes survivin, a member of the inhibitor of apoptosis protein family, which is highly expressed by most cancers and associated with chemotherapy resistance, increased tumor recurrence, and shorter patient survival, making anti-survivin therapy an attractive cancer treatment strategy (33).

Because of the modular nature of our agent, the described method is not only novel but also highly relevant to a variety of neoplastic and other diseases that can be manipulated at the level of gene expression. Ultimately, we believe that the core elements of the developed technology would be applicable in a clinical setting because related iron oxides are already in clinical use (34).

Disclosure of Potential Conflicts of Interest

No potential conflicts of interest were disclosed.

Acknowledgments

We thank Pamela Pantazopoulos for help with the *in vitro* and *ex vivo* studies.

Grant Support

NIH grant R00CA129070 (Z. Medarova).

The costs of publication of this article were defrayed in part by the payment of page charges. This article must therefore be hereby marked *advertisement* in accordance with 18 U.S.C. Section 1734 solely to indicate this fact.

Received 06/08/2010; revised 07/24/2010; accepted 07/30/2010; published OnlineFirst 08/11/2010.

References

1. Dykxhoorn DM, Lieberman J. The silent revolution: RNA interference as basic biology, research tool, and therapeutic. Annu Rev Med 2005;56:401–23.
2. Song E, Lee SK, Wang J, et al. RNA interference targeting Fas protects mice from fulminant hepatitis. Nat Med 2003;9:347–51.
3. Brummelkamp TR, Bernards R, Agami R. Stable suppression of tumorigenicity by virus-mediated RNA interference. Cancer Cell 2002;2:243–7.
4. Judge AD, Sood V, Shaw JR, Fang D, McClintock K, MacLachlan I. Sequence-dependent stimulation of the mammalian innate immune response by synthetic siRNA. Nat Biotechnol 2005;23:457–62.
5. Takeshita F, Minakuchi Y, Nagahara S, et al. Efficient delivery of small interfering RNA to bone-metastatic tumors by using atelocollagen *in vivo*. Proc Natl Acad Sci U S A 2005;102:12177–82.
6. Takeshita F, Ochiya T. Therapeutic potential of RNA interference against cancer. Cancer Sci 2006;97:689–96.
7. Howard KA, Rahbek UL, Liu X, et al. RNA interference *in vitro* and *in vivo* using a novel chitosan/siRNA nanoparticle system. Mol Ther 2006;14:476–84.
8. Pille JY, Li H, Blot E, et al. Intravenous delivery of anti-RhoA small interfering RNA loaded in nanoparticles of chitosan in mice: safety and efficacy in xenografted aggressive breast cancer. Hum Gene Ther 2006;17:1019–26.
9. Kumar P, Wu H, McBride JL, et al. Transvascular delivery of small interfering RNA to the central nervous system. Nature 2007;448:39–43.
10. Song EY, VanDunk C, Kuddo T, Nelson PG. Measurement of vasoactive intestinal peptide using a competitive fluorescent microsphere immunoassay or ELISA in human blood samples. J Immunol Methods 2005;300:63–73.
11. Peer D, Zhu P, Carman CV, Lieberman J, Shimaoka M. Selective gene silencing in activated leukocytes by targeting siRNAs to the integrin lymphocyte function-associated antigen-1. Proc Natl Acad Sci U S A 2007;104:4095–100.
12. Akita H, Kogure K, Moriguchi R, et al. Nanoparticles for *ex vivo* siRNA delivery to dendritic cells for cancer vaccines: programmed endosomal escape and dissociation. J Control Release 2010;143:311–7.
13. Patnaik S, Arif M, Pathak A, Kurupati R, Singh Y, Gupta K. Cross-linked polyethylenimine-hexametaphosphate nanoparticles to deliver nucleic acids therapeutics. Nanomedicine 2010;6:344–54.
14. Kaneda M, Sasaki Y, Lanza G, Milbrandt J, Wickline S. Mechanisms of nucleotide trafficking during siRNA delivery to endothelial cells using perfluorocarbon nanoemulsions. Biomaterials 2010;31:3079–86.
15. Chen Y, Wu J, Huang L. Nanoparticles targeted with NGR motif deliver c-myc siRNA and doxorubicin for anticancer therapy. Mol Ther 2010;18:828–34.
16. Li J, Chen Y, Tseng Y, Mozumdar S, Huang L. Biodegradable calcium phosphate nanoparticle with lipid coating for systemic siRNA delivery. J Control Release 2010;142:416–21.
17. Gao W, Xiao Z, Radovic-Moreno A, Shi J, Langer R, Farokhzad O. Progress in siRNA delivery using multifunctional nanoparticles. Methods Mol Biol 2010;629:53–67.
18. Massoud TF, Gambhir SS. Molecular imaging in living subjects: seeing fundamental biological processes in a new light. Genes Dev 2003;17:545–80.
19. Lee J, Lee K, Moon S, Lee Y, Park T, Cheon J. All-in-one target-cell-specific magnetic nanoparticles for simultaneous molecular imaging and siRNA delivery. Angew Chem Int Ed Engl 2009;48:4174–9.
20. Medarova Z, Pham W, Farrar C, Petkova V, Moore A. *In vivo* imaging of siRNA delivery and silencing in tumors. Nat Med 2007;13:372–7.
21. Mikhaylova M, Stasinopoulos I, Kato Y, Artemov D, Bhujwalla ZM.

Imaging of cationic multifunctional liposome-mediated delivery of COX-2 siRNA. Cancer Gene Ther 2009;16:217–26.
22. Krishnamachary B, Glunde K, Wildes F, et al. Noninvasive detection of lentiviral-mediated choline kinase targeting in a human breast cancer xenograft. Cancer Res 2009;69:3464–71.
23. Moore A, Medarova Z, Potthast A, Dai G. *In vivo* targeting of underglycosylated MUC-1 tumor antigen using a multimodal imaging probe. Cancer Res 2004;64:1821–7.
24. Medarova Z, Pham W, Kim Y, Dai G, Moore A. *In vivo* imaging of tumor response to therapy using a dual-modality imaging strategy. Int J Cancer 2006;118:2796–802.
25. Medarova Z, Rashkovetsky L, Pantazopoulos P, Moore A. Multiparametric monitoring of tumor response to chemotherapy by noninvasive imaging. Cancer Res 2009;69:1182–9.
26. Medarova Z, Evgenov NV, Dai G, Bonner-Weir S, Moore A. *In vivo* multimodal imaging of transplanted pancreatic islets. Nat Protoc 2006;1:429–35.
27. Medarova Z, Kumar M, Ng SW, Moore A. Development and application of a dual-purpose nanoparticle platform for delivery and imaging of siRNA in tumors. Methods Mol Biol 2009;555:1–13.
28. Hogemann D, Josephson L, Weissleder R, Basilion JP. Improvement of MRI probes to allow efficient detection of gene expression. Bioconjug Chem 2000;11:941–6.
29. Fire A, Xu S, Montgomery MK, Kostas SA, Driver SE, Mello CC. Potent and specific genetic interference by double-stranded RNA in *Caenorhabditis elegans*. Nature 1998;391:806–11.
30. Elbashir SM, Harborth J, Lendeckel W, Yalcin A, Weber K, Tuschl T. Duplexes of 21-nucleotide RNAs mediate RNA interference in cultured mammalian cells. Nature 2001;411:494–8.
31. Tiemann K, Rossi JJ. RNAi-based therapeutics—current status, challenges and prospects. EMBO Mol Med 2009;1:142–51.
32. Perey L, Hayes DF, Maimonis P, Abe M, O'Hara C, Kufe DW. Tumor selective reactivity of a monoclonal antibody prepared against a recombinant peptide derived from the DF3 human breast carcinoma-associated antigen. Cancer Res 1992;52:2563–8.
33. Fukuda S, Pelus LM. Survivin, a cancer target with an emerging role in normal adult tissues. Mol Cancer Ther 2006;5:1087–98.
34. Harisinghani MG, Barentsz J, Hahn PF, et al. Noninvasive detection of clinically occult lymph-node metastases in prostate cancer. N Engl J Med 2003;348:2491–9.